Supporting Information

Correlating Oxidation State and Surface Area to Activity from *Operando* Studies of Copper CO Electroreduction Catalysts in a Gas-fed Device

Soo Hong Lee,[†,#] Ian Sullivan,[‡,#] David M. Larson,[†] Guiji Liu,[†]
Francesca M. Toma,[†] Chengxiang Xiang,[*,‡] and Walter S. Drisdell[*,†]

[†]*Joint Center for Artificial Photosynthesis and Chemical Sciences Division, Lawrence Berkeley National Laboratory, 1 Cyclotron Rd., Berkeley, California 94720, United States.*
[‡]*Joint Center for Artificial Photosynthesis and Division of Chemistry and Chemical Engineering, California Institute of Technology, 1200 E. California Blvd., Pasadena, California 91125, United States.*

[#]*These authors contributed equally to this work.*

Corresponding Author
*E-mail: wsdrisdell@lbl.gov; cxx@caltech.edu

Experimental Section

Over-absorption correction and linear combination fitting. The thickness of prepared Cu catalysts is larger than the required thickness for X-ray transmission detection. Instead, XAS spectra can be obtained by measuring the yield of fluorescent photons (fluorescence yield detection), but this detection can result in distorted spectra due to absorption effects in a concentrated sample.[S1] The distorted spectra induced by over-absorption were corrected in the following manner. This model supposes that the smooth part of the resonant absorption ($\mu_{resonant}$) comes from a constant fraction of the non-resonant background ($\mu_{non-resonant}$) and fluorescence ($\mu_{fluorescence}$), which is a proper as2sumption in the XANES region. This assumption leads us to adopt an over-absorption parameter (a) as follows:

$$a = \mu_{resonant} / (\mu_{non-resonant} + \mu_{fluorescence})$$

The sample in this model is assumed to be infinitely thick such that all incident X-ray photons are absorbed. When we consider the energy range and size of the sample compared to beam size, the model uses a simple equation as follows:

$$y_{corrected} = y_{exp} / (1 + a(1 - y_{exp})$$

where y_{exp} and $y_{corrected}$ are the normalized resonant absorbance observed in experiments and over-absorption corrected absorbance, respectively.[S2] The parameter a increases as the over-absorption effect increases and can be adjusted to obtain the best fitting results between the corrected spectrum and experimental spectra. The fitting error on each spectrum was estimated by using three different values of a, resuting in variation in the composition of oxides.

Linear combination fitting (LCF) of XANES spectra was performed using Cu, Cu_2O, CuO, and $Cu(OH)_2$ reference spectra, representing Cu^0, Cu^{1+}, and Cu^{2+} oxidation states. The obtained *operando* XANES spectra are fitted by a weighted sum of all the reference spectra with the fraction of species restricted to be non-negative. The quality of the fits was estimated by calculating normalized sum-squares (NSS) residuals in the range of 8950~9150 eV as follows:

$$NSS = \sum (y_{exp} - y_{fit})^2 / \sum (y_{ex})^2 \times 100$$

An energy shift of ± 1 eV at maximum and a correction of the slope were allowed to address an issue relating to the energy resolution of the monochromator. All the XAS data processing was conducted using LabView programs available online at https://sites.google.com/lbl.gov/lbnl-als-1032/ (Dr. Matthew A. Marcus).
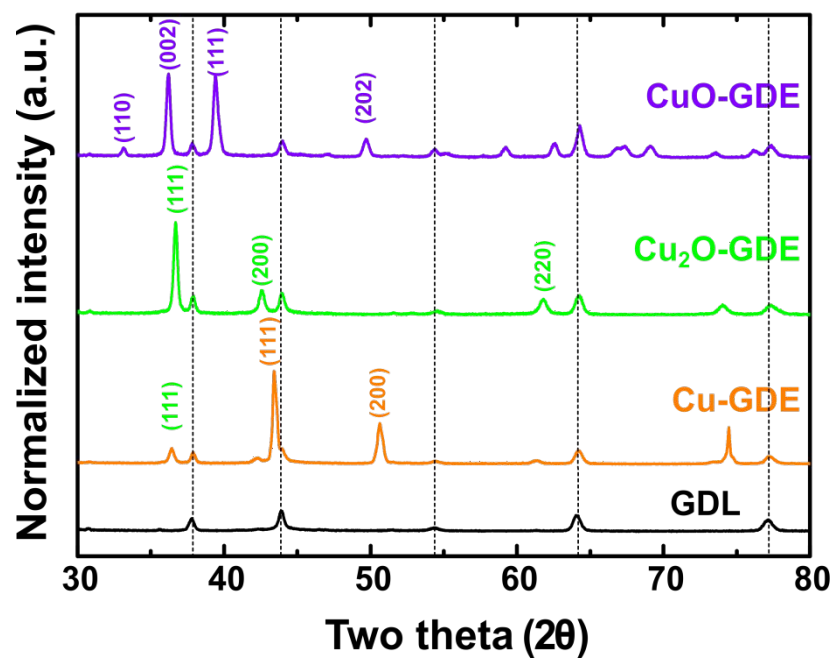
Figure S1. XRD patterns of the Cu catalysts, and GDL. The XRD patterns of Cu catalysts can be indexed to the characteristic diffraction peaks of Cu, Cu_2O, and CuO, respectively. The black dotted lines represent the GDL diffraction peaks, which were detected in all Cu catalysts.
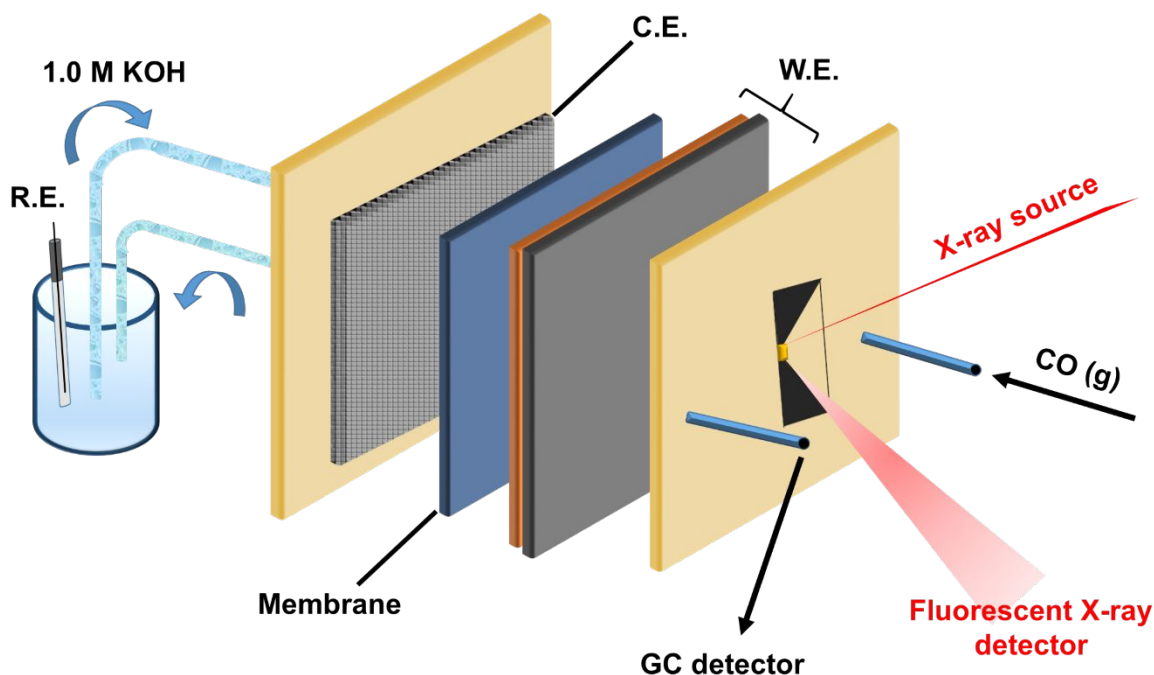
Figure S2. An experimental set-up for an *operando* X-ray absorption spectroscopy (XAS) cell. A hybrid catalyst-bonded membrane device was slightly modified with a window composed of X-ray transparent polyimide tape. A Pt mesh was utilized as a counter electrode (C.E.), and 1.0 M KOH electrolyte circulated in the anode chamber. In the cathode chamber, Cu catalysts, including Cu-GDE, Cu_2O-GDE, and CuO-GDE were used as a working electrode (W.E.), and CO gas was introduced at a flow rate of 10 sccm. The two chambers were separated by anion exchange membrane. The Ag/AgCl reference electrode (R.E.) was placed in the anolyte reservoir due to the absence of electrolyte in the cathode chamber.
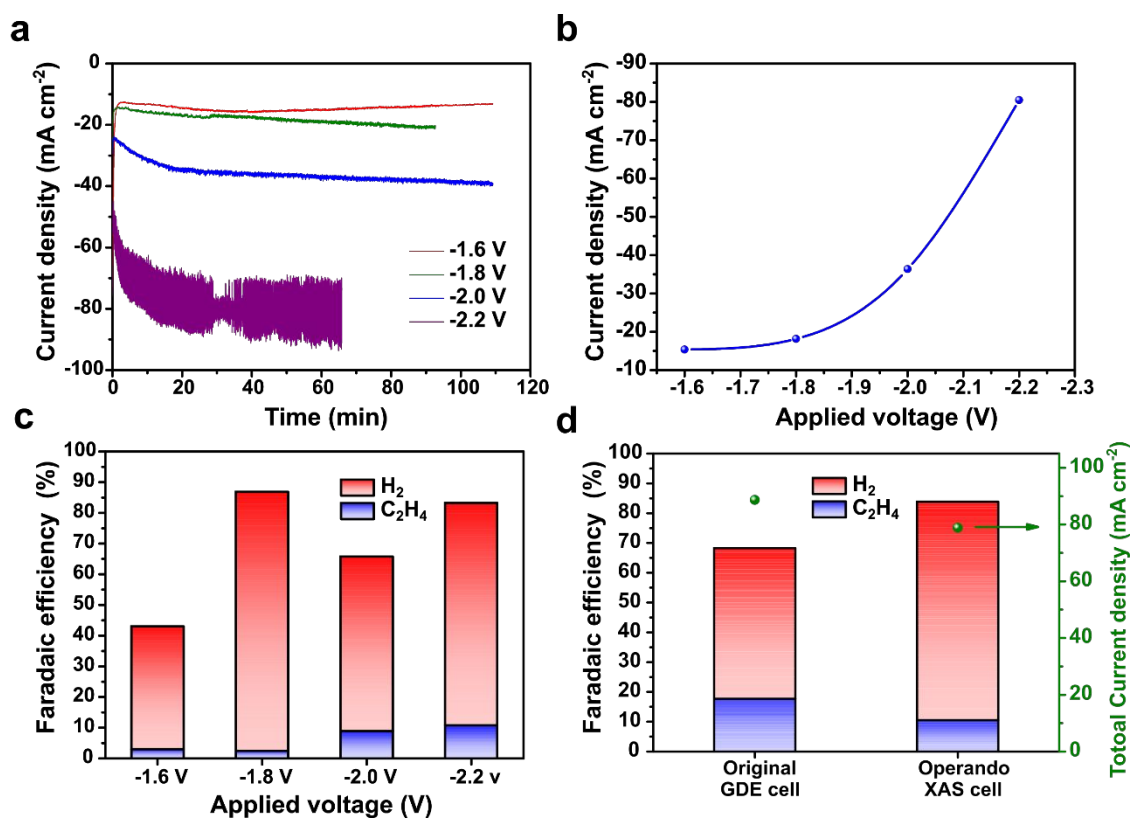
Figure S3. CO reduction performance of Cu-GDE in the *operando* XAS cell. (a) Temporal changes in the total current density of Cu-GDE as a function of applied potential. (b) Total current density versus the applied potential for CORR on Cu-GDE normalized to the geometric surface area. (c) Corresponding Faradaic efficiency (FE) of H_2 and C_2H_4 for Cu-GDE. (d) Comparison of CORR performance in original gas-fed GDE cell and *operando* XAS cell. The negative potential of -2.2 V vs. Ag/AgCl was applied for 1 hr toward the Cu-GDE in both cells. In the case of *operando* XAS cell, only gas products (C_2H_4 and H_2) were characterized due to synchronized measurements between XAS and GC. Liquid product characterization in the original GDE cell is displayed in Figure S13.
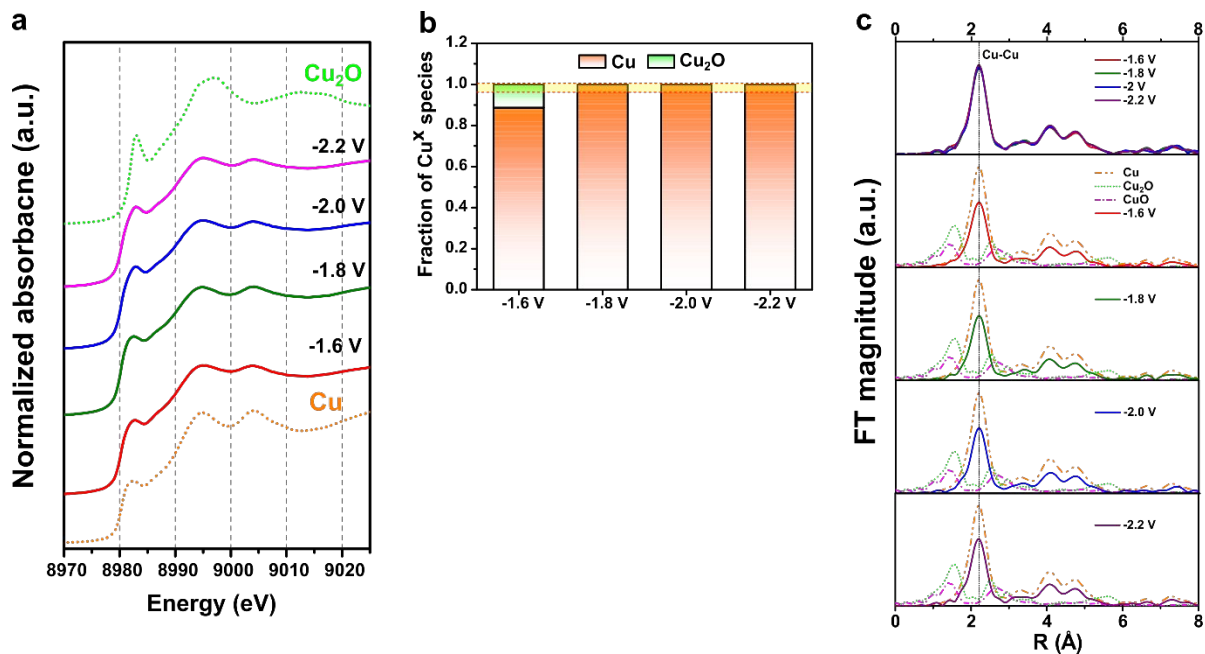
Figure S4. *Operando* XAS data. (a) *operando* Cu K-edge XANES spectra of Cu-GDE at different applied potentials (solid lines) and *ex-situ* XANES spectra of standard Cu metal (orange dotted) and Cu_2O (green dotted). (b) The calculated ratio of Cu oxidation states from linear combination fitting (LCF) as a function of the applied potential. The yellow shaded region represents the estimated error range of up to 4% in the LCF analysis. (c) Corresponding k^2-weighted Fourier transformed Cu EXAFS data as a function of applied potential.
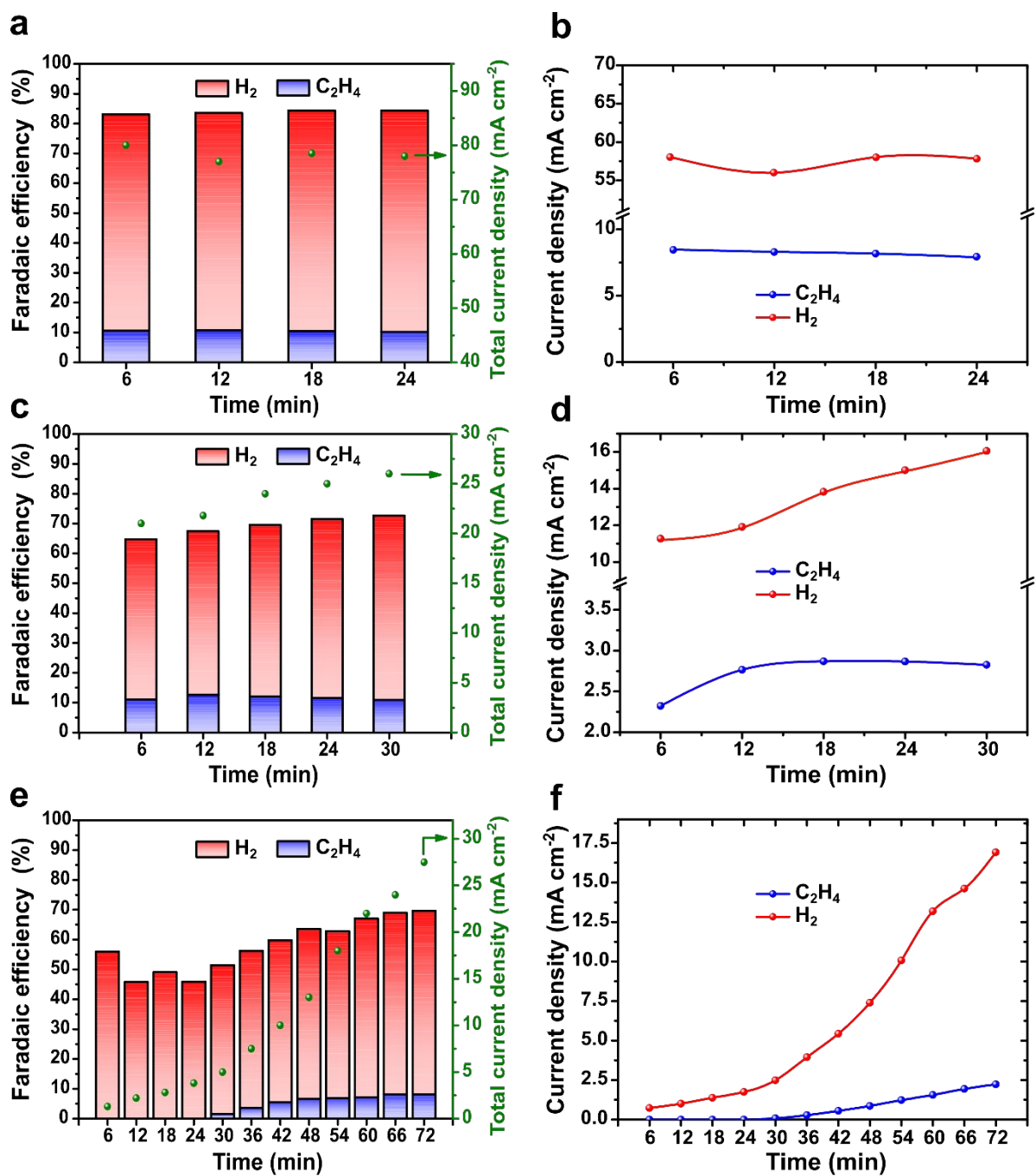
Figure S5. CORR performance of Cu catalysts in the *operando* XAS cell. FE and partial current densities of Cu-GDE (a and b), Cu_2O-GDE (c and d), and CuO-GDE (e and f) for H_2 (red) and C_2H_4 (blue). Measurements of GC and XAS were synchronized and collected every 6 min during electrolysis at -2.2 V vs. Ag/AgCl.
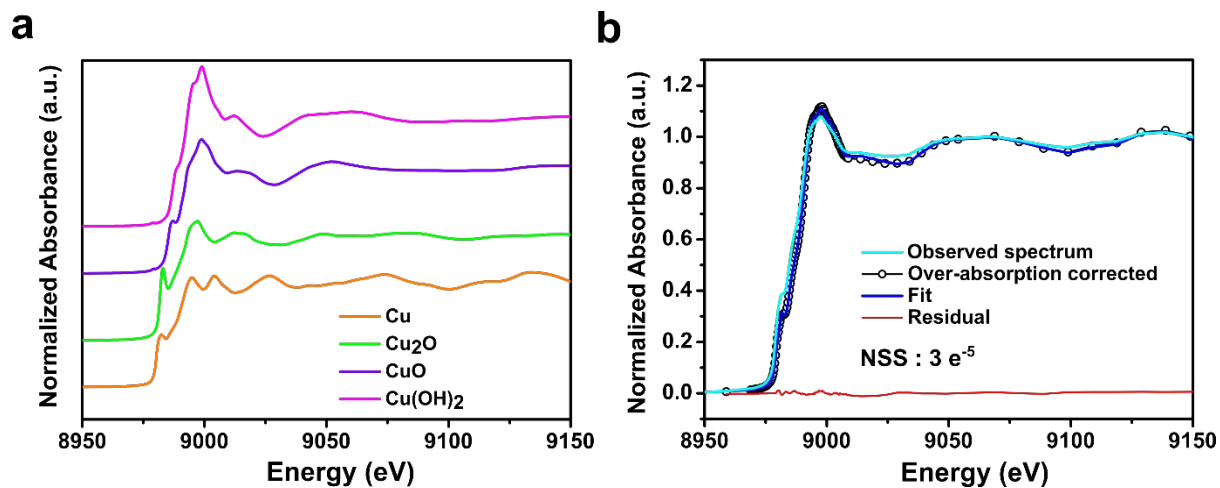
Figure S6. LCF analysis of XANES spectra. (a) XANES spectra on Cu K-edge of the standard Cu metal, Cu_2O, CuO, and $Cu(OH)_2$ that used for LCF analysis. (b) Representative LCF analysis of the *operando* XANES spectrum of CuO-GDE during CORR at -2.2 V vs. Ag/AgCl.
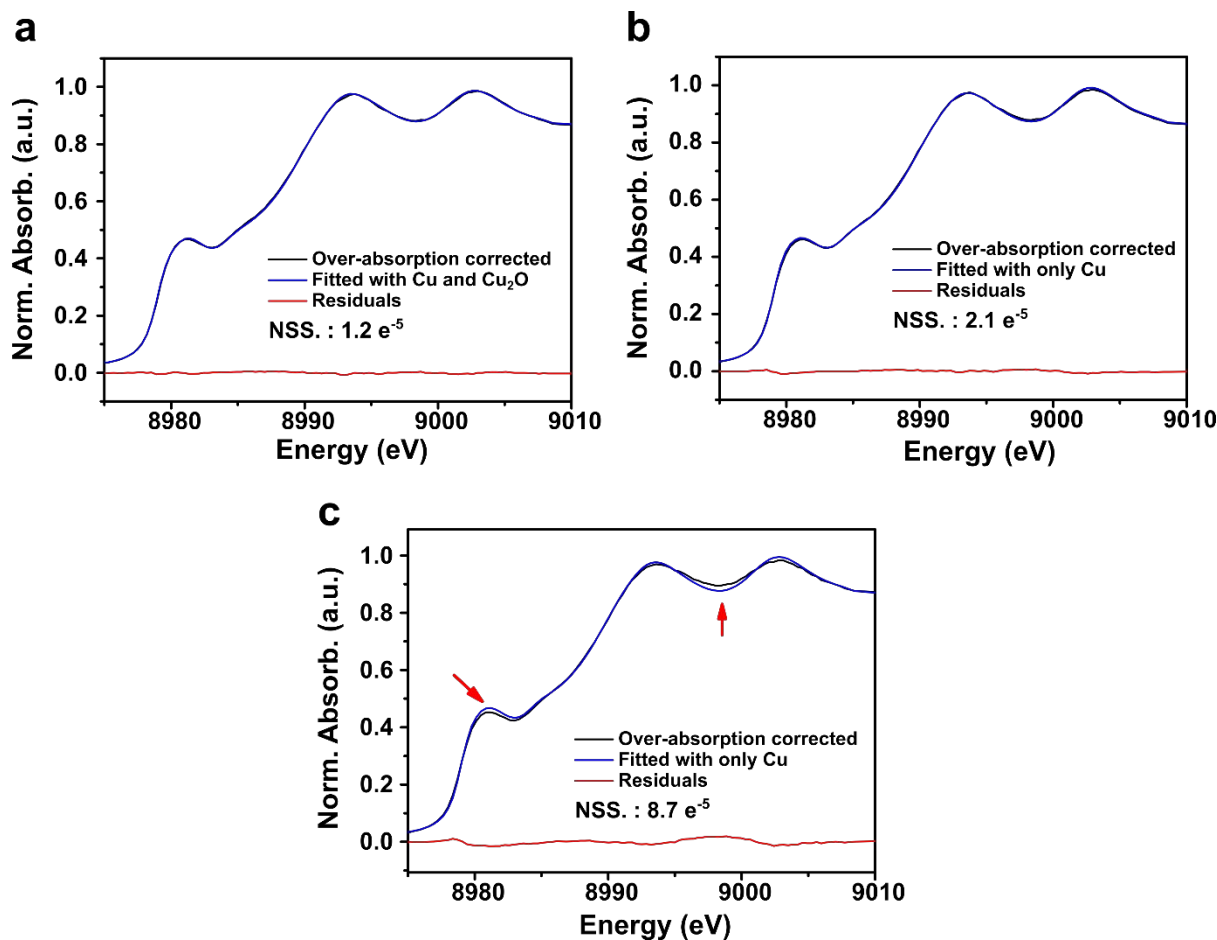
Figure S7. Error estimation of the LCF analysis. (a) *Operando* XANES spectrum of Cu_2O-GDE after 30 min of CORR and its best-fit with a linear combination of standard Cu metal and Cu_2O. (b) Same XANES spectrum as (a) and its best-fit with only a standard Cu metal. Excluding 3.7 % of Cu_2O does not result in a viable mismatching between over-absorption corrected data and fitted spectrum. (c) *Operando* XANES spectrum of Cu_2O-GDE after 24 min of CORR and its best-fit with only a standard Cu metal. Red arrows indicated a viable mismatch between observed and fitted data.

The error of LCF analysis originates from inevitable uncertainty in the slope of the post-edge line during the normalization process.[S3] To evaluate a reasonable error margin, we introduced the empirical method to delineate the error margin by using NSS as a best-fit criterion. A validation of this method can be obtained by comparing the fitting results of the above sample (Cu_2O-GDE after 30 min). Although the inclusion of ~3.7 % of Cu_2O reference to fitting parameters further decreases the NSS value, the fitted spectra without Cu_2O reference did not show any mismatch from the corrected data (Figures S7a and S7b). In contrast, the sample

(Cu$_2$O-GDE after 24 min) with ~4.8% of Cu-oxide from LCF exhibited a clear mismatch when the spectrum was fitted without any Cu-oxide references (Figure S7c). We conclude that the accuracy for the determination of Cu oxidation states via LCF analysis is within 3-4%.

.
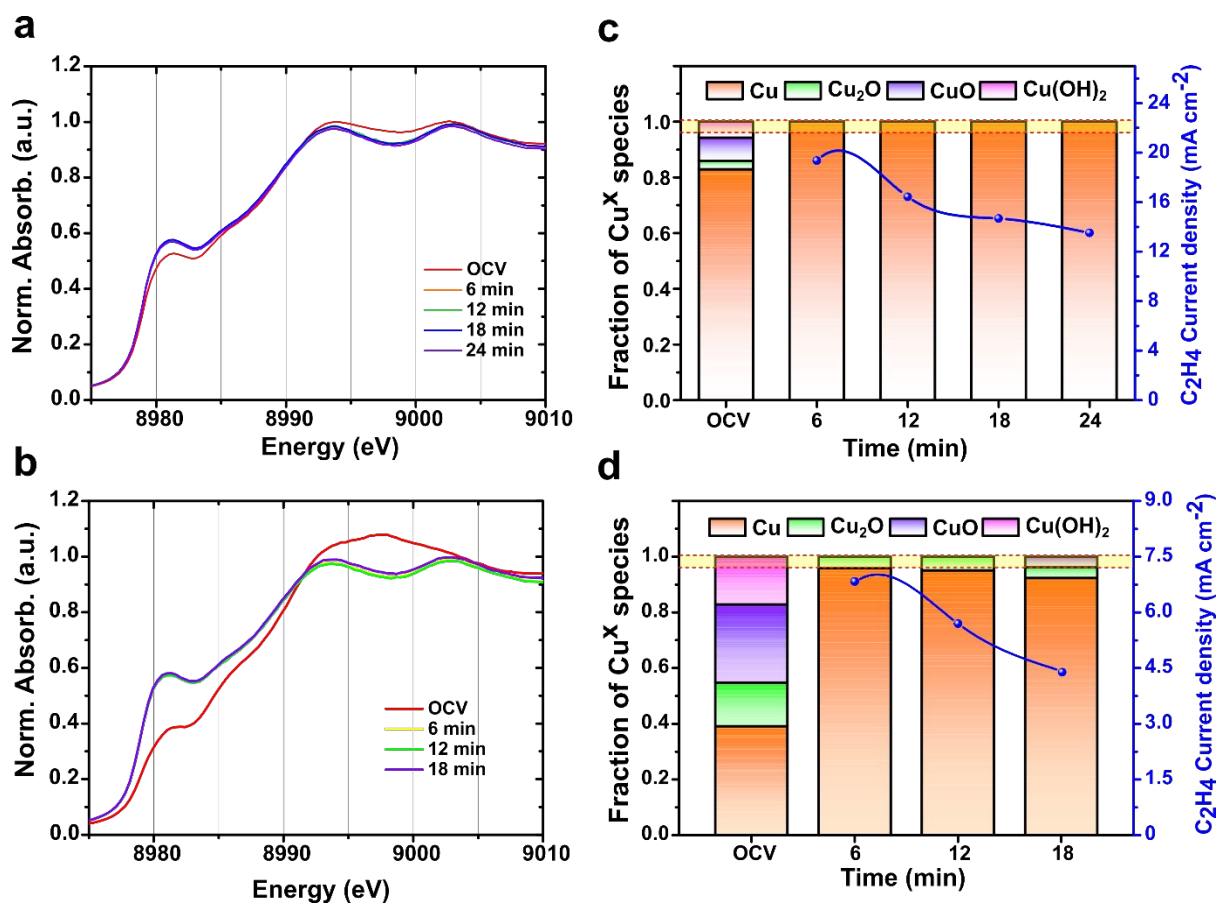
Figure S8. *Operando* XANES spectra after electrochemical oxidation. Temporal changes of Cu K-edge XANES spectra of Cu-GDE (a) and CuO-GDE (b) after applying anodic potential at 1.5 V vs. Ag/AgCl for 5min. The calculated ratio of Cu oxidation states of Cu-GDE (c) and CuO-GDE (d) derived from LCF analysis as a function of CORR time. The yellow shaded region represents the estimated error range of up to 4% in the LCF analysis.

S12
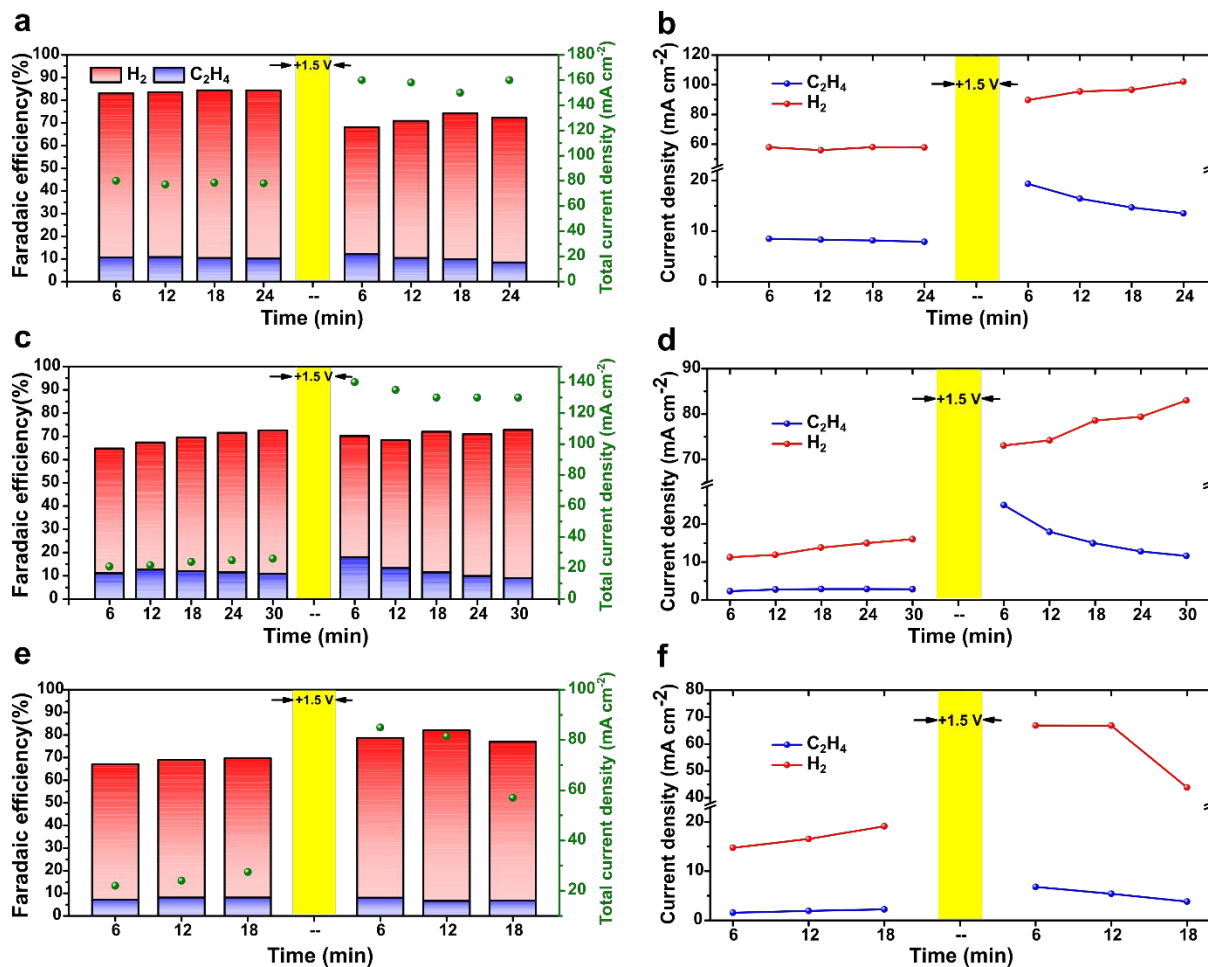
Figure S9. CORR performance of Cu catalysts in the *operando* XAS cell before and after electrochemical oxidation. FE and partial current densities of Cu-GDE (a and b), Cu$_2$O-GDE (c and d), and CuO-GDE (e and f) for H$_2$ (red) and C$_2$H4 (blue). Measurements of GC and XAS were synchronized and collected every 6 min during electrolysis at -2.2 V vs. Ag/AgCl. The yellow regions represent the electrochemical oxidation period that applied 1.5 V vs. Ag/AgCl for 5 min. Due to the slow initial reduction of CuO-GDE, panels e and f show only the end of the reduction period, starting at 60 min.
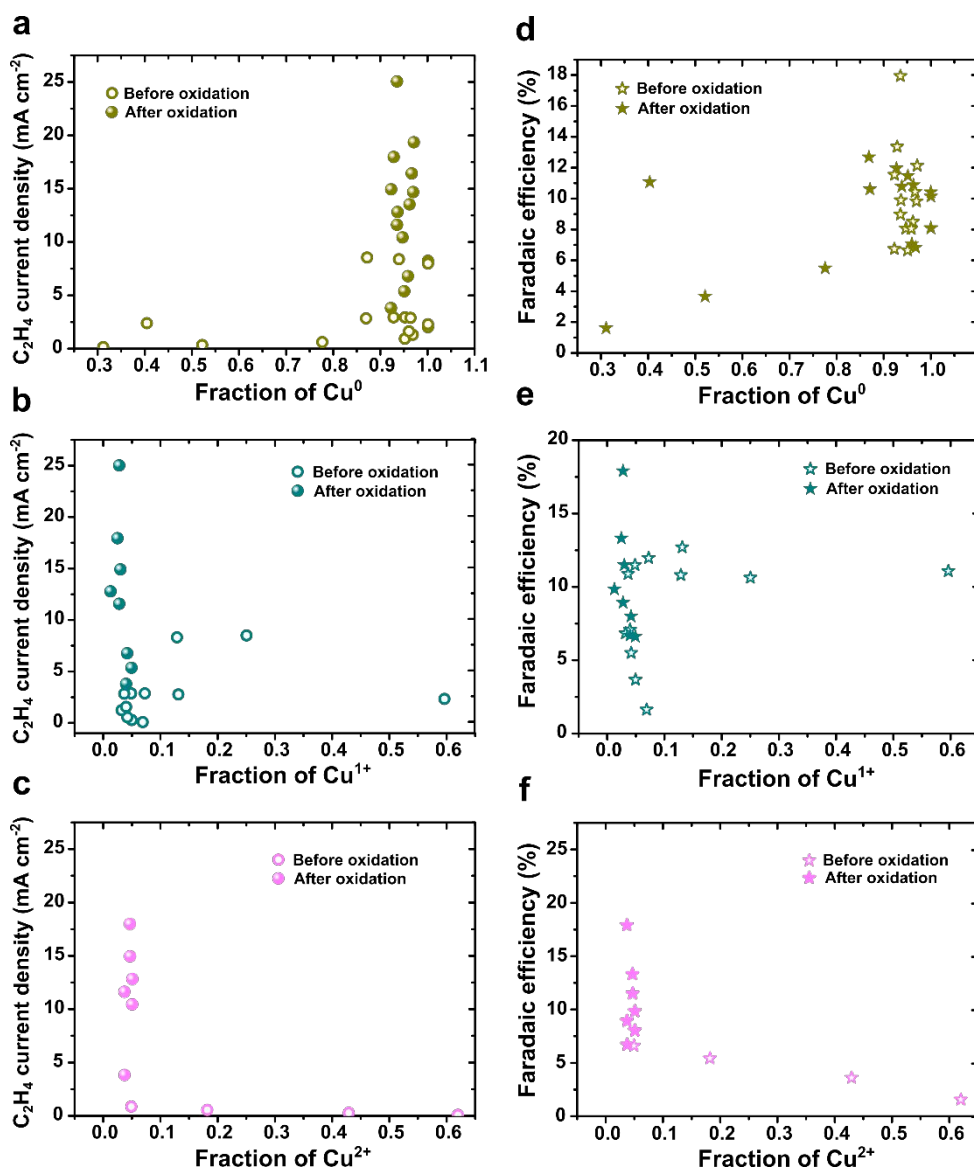
Figure S10. Relationship between specific Cu ion species (Cu^0, Cu^+, and Cu^{2+}) and CORR performance. (a~c) C_2H_4 partial current densities as a function of the fraction of Cu^0 (a), Cu^+ (b), and Cu^{2+} (c). (d~f) Faradaic efficiency for C_2H_4 as a function of the fraction of Cu^0 (d), Cu^+ (e), and Cu^{2+} (f). The calculated percentage of each Cu ion species through LCF analysis is directly linked to the observed C_2H_4 partial current density and Faradaic efficiency that were measured at the same time when the corresponding XAS spectra obtained.
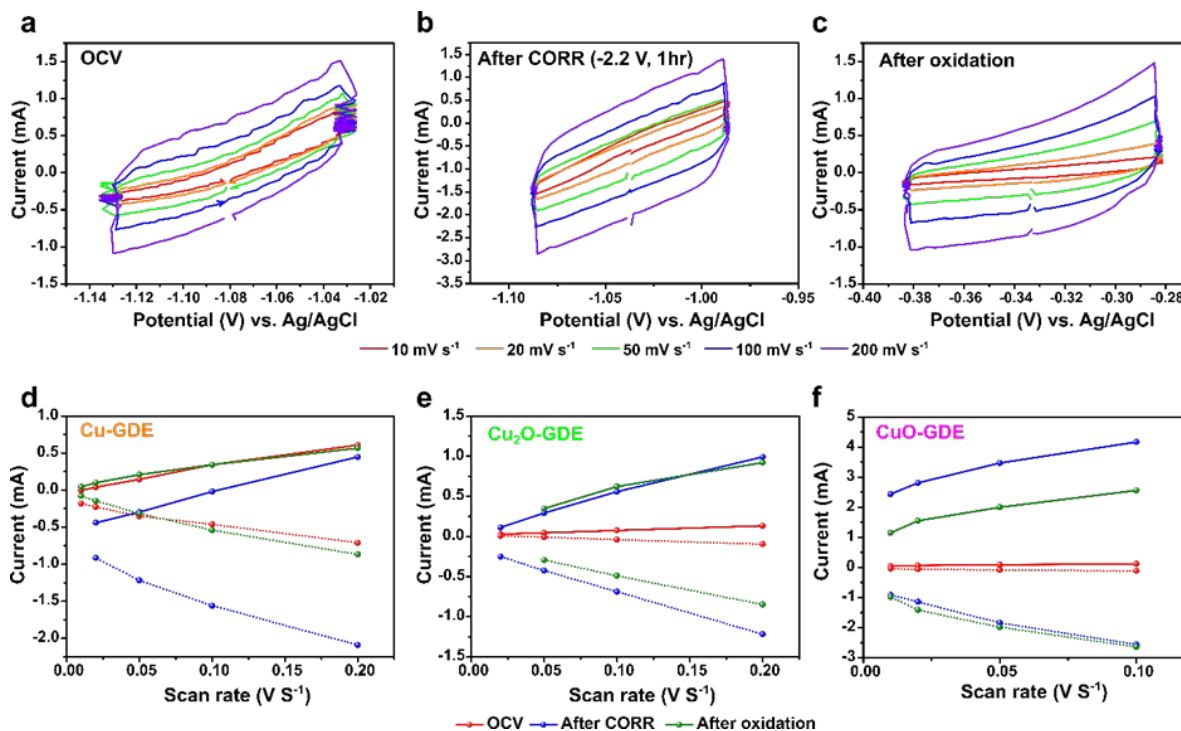
Figure S11. Estimation of electrochemical surface area (ECSA) in model catalysts. (a~c) Electrochemical double-layer capacitance (EDLC) analysis of Cu-GDE at OCV before electrolysis (a), after CORR at -2.2 V vs. Ag/AgCl for 1hr (b), and after electrochemical oxidation at 1.5 V vs. Ag/AgCl for 5 min (c). Capacitance currents were plotted as a function of applied potential with various scan rates. (d~f) Capacitance currents as a function of the scan rate of Cu-GDE (d), Cu_2O-GDE (e), and CuO-GDE (f). The slope of this graph gives the EDLC values.

Before the CORR, the Cu_2O-GDE and CuO-GDE showed significantly lower EDLC values than that of Cu-GDE, attributed to the fact that Cu_2O is intrinsically hydrophobic,[S4] and a calcination step for CuO-GDE can remove surface hydroxyl groups,[S5] respectively. All the EDLC of Cu catalysts decreased slightly after anodic oxidation. This decrease may be attributed to the change of wettability in the catalyst layer due to the formation of a hydrophobic Cu_2O surface in response to anodic potentials, but still needs more detailed mechanistic study. We note that the EDLC measurements yield an ECSA that may include contributions from the GDL in addition to the catalyst, which can lead to an underestimation of the C_2H_4 activity. We expect near total coverage of the GDL by the catalyst, however, so the EDLC measurements should yield a good approximation of the ECSA.
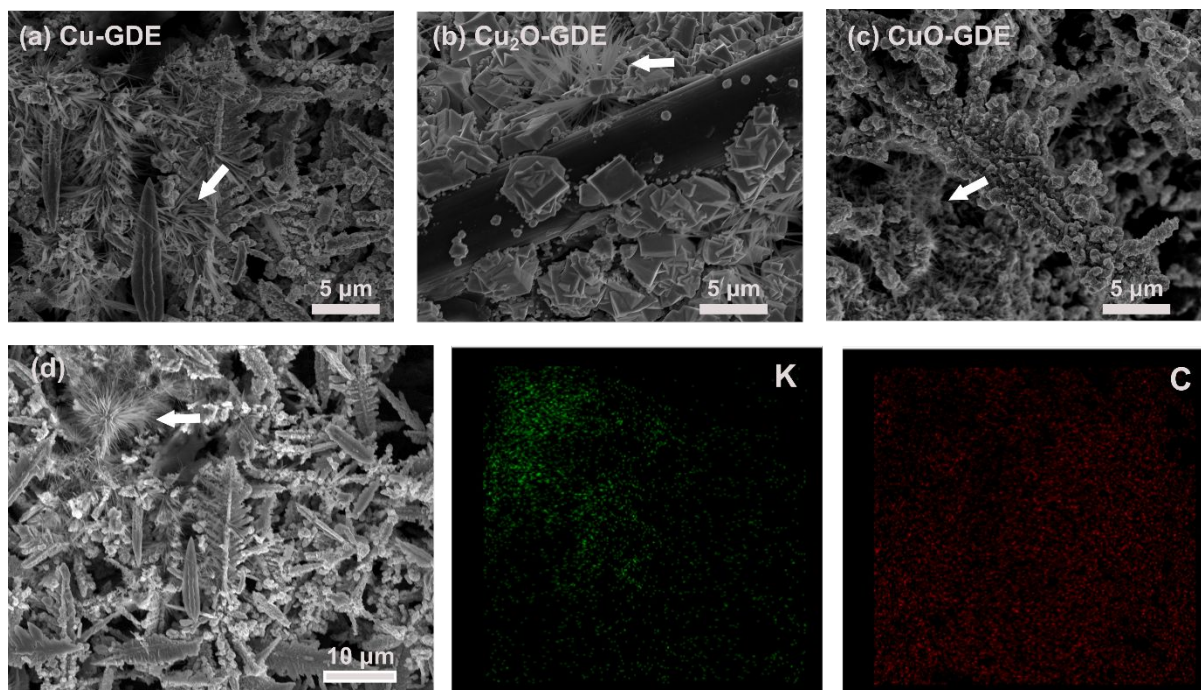
Figure S12. KOH salt deposition on the cathode. (a~c) *Ex-situ* and post-mortem SEM images of Cu-GDE (a), Cu$_2$O-GDE (b), and CuO-GDE (c) operated at -2.2 V vs. Ag/AgCl for 30 min. White arrows in the panel a,b, and c indicate KOH salt deposition with a spindle shape. (d) EDX mapping of Cu-GDE after CORR for 1 h (2.2 V vs. Ag/AgCl). The potassium (K) signal was observed in the Cu surface, and the carbon (C) signal represented GDL.
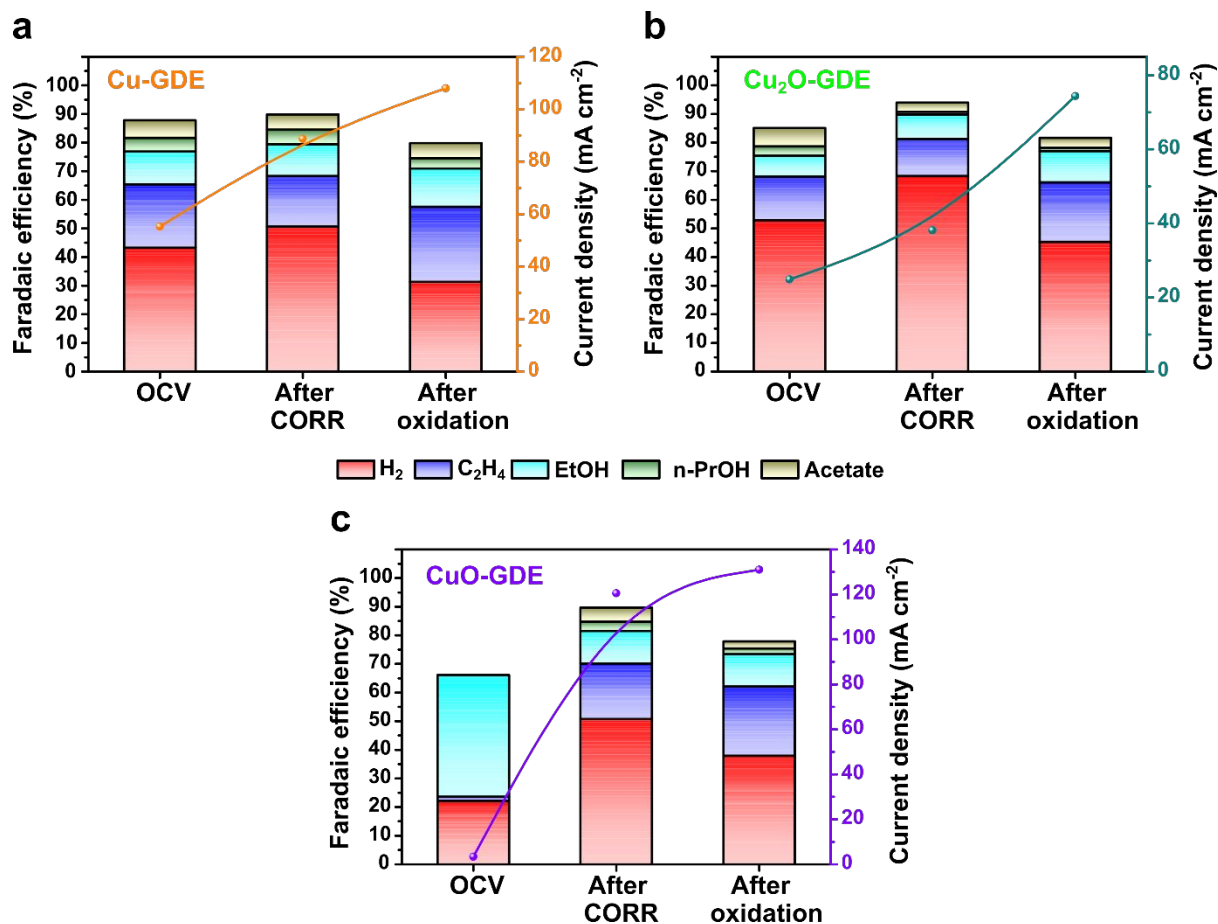
Figure S13. CORR performance of three Cu catalysts in the original gas-fed cell. (a-c) Total current density and cumulative FE of Cu-GDE (a), Cu$_2$O-GDE (b), and CuO-GDE (c) at -2.2 V vs. Ag/AgCl. The CORR performance was estimated at the same points where the corresponding EDLCs were measured. At OCV, the total currents and FE were characterized 6 min after EDLC was measured. "After CORR" represents CORR performance at -2.2 V vs. Ag/AgCl after 1hr, and "after oxidation" represents CORR performance after electrochemical oxidation at 1.5 V vs. Ag/AgCl for 5 min.
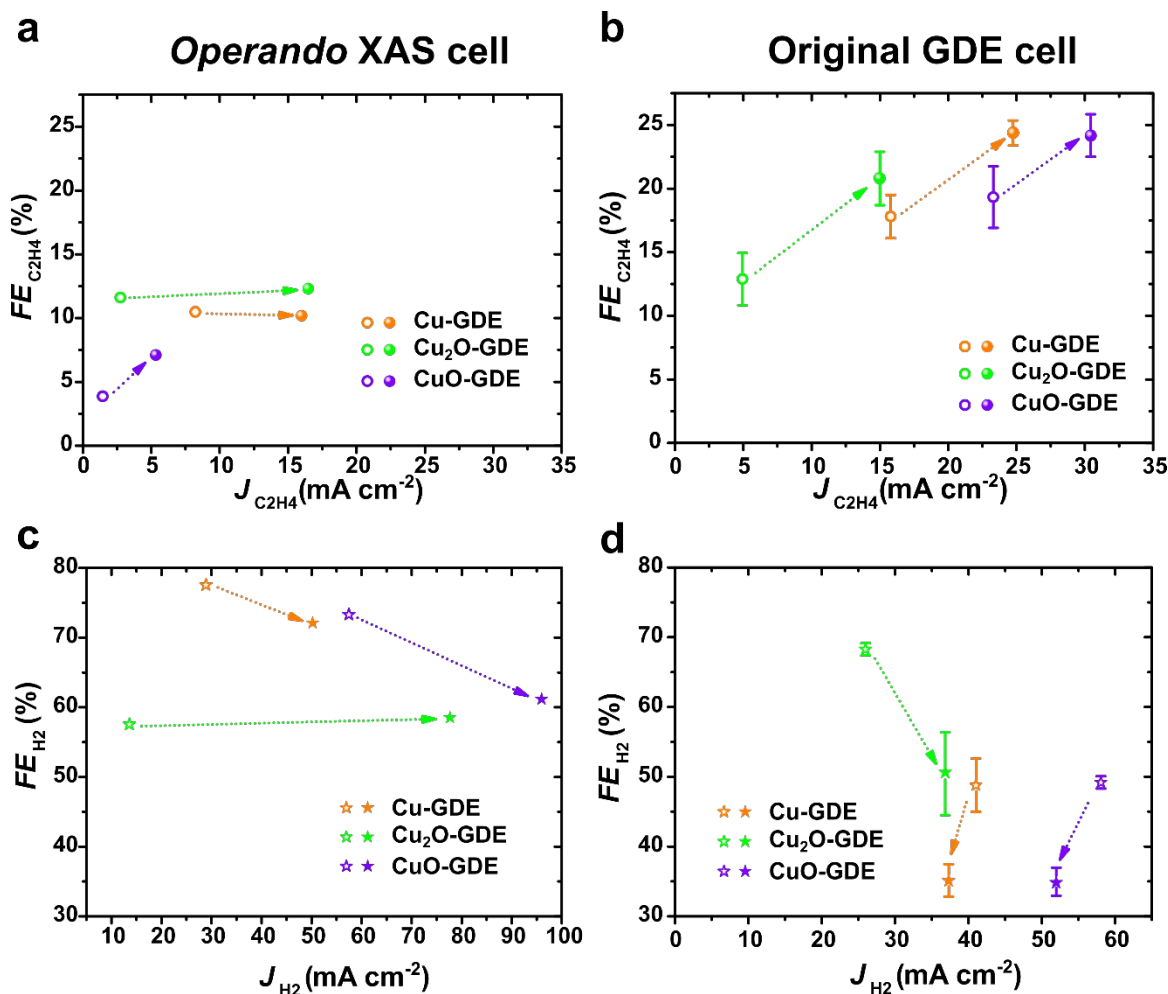
**Figure S14.** Comparison of the selectivity and activity for H_2 and C_2H_4 production of Cu catalysts in the *operando* XAS cell and original gas-fed cell. FE of C_2H_4 (FE_{C2H4}) as a function of partial current density (J_{C2H4}) in the *operando* XAS cell (a) and original gas-fed cell (b) before (empty circle) and after (filled circle) electrochemical oxidation. FE of H_2 (FE_{H2}) as a function of partial current density (J_{H2}) in the *operando* XAS cell (c) and original gas-fed cell (d) before (empty star) and after (filled star) electrochemical oxidation. Error bars represent the standard deviation from three independent measurements. All the FE and partial current densities were averaged throughout the whole measurement period.

To study the effects of the window modification on the CORR activity and selectivity in gas-fed cells, we compared the CORR performance of the gas-fed and *operando* XAS cells before and after anodic oxidation. In the gas-fed cell, both C_2H_4 partial current densities and FE_{C2H4} were increased higher than that of the *operando* XAS cell, while both H_2 partial current

densities and FE_{H2} were decreased significantly, except for the partial current densities of the Cu_2O-GDE. These differences suggest that the window in the *operando* XAS cell cannot efficiently compress the cathode, making it more permeable to electrolytes from the anode side. Such enhanced penetration of the electrolyte could result in water flooding in the catalyst layer so that the rate of HER is higher relative to that of the original gas-fed cell. From this result, it is not safe to assume that even a minor modification of the cell design will not change the catalyst environments.
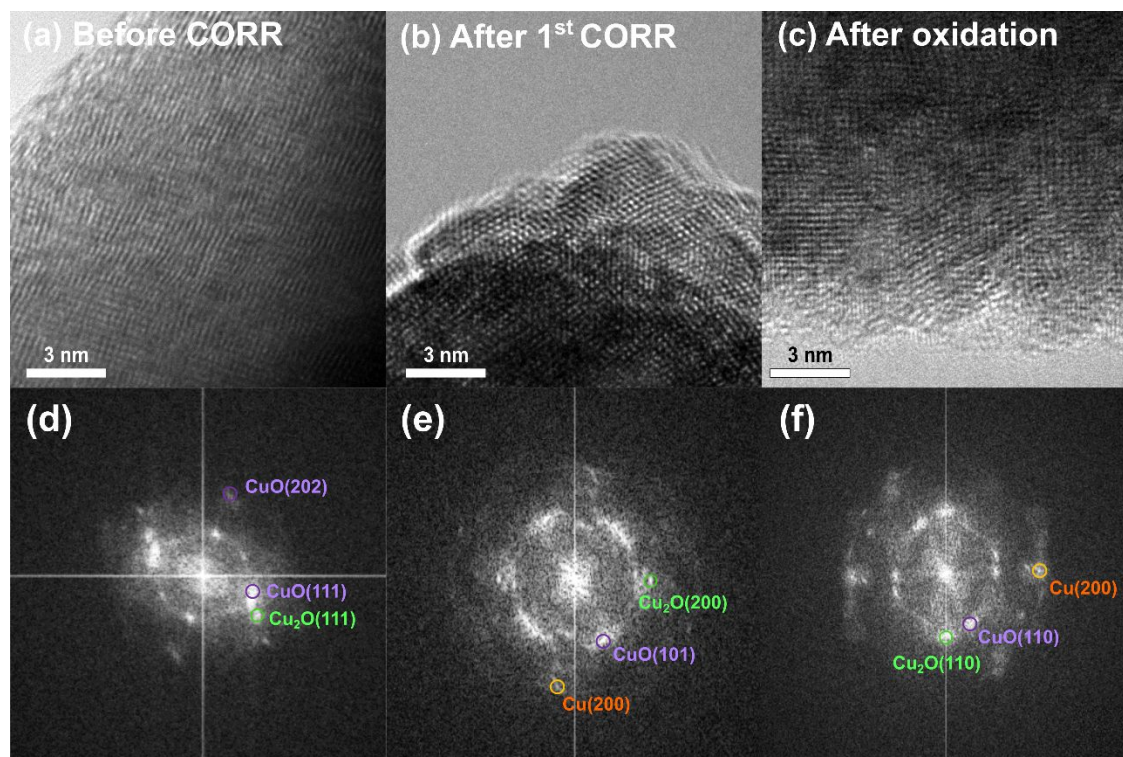
Figure S15. *Ex-situ* TEM analysis of Cu-GDE before and after CORR and subsequent electrochemical oxidation. (a~c) High-resolution 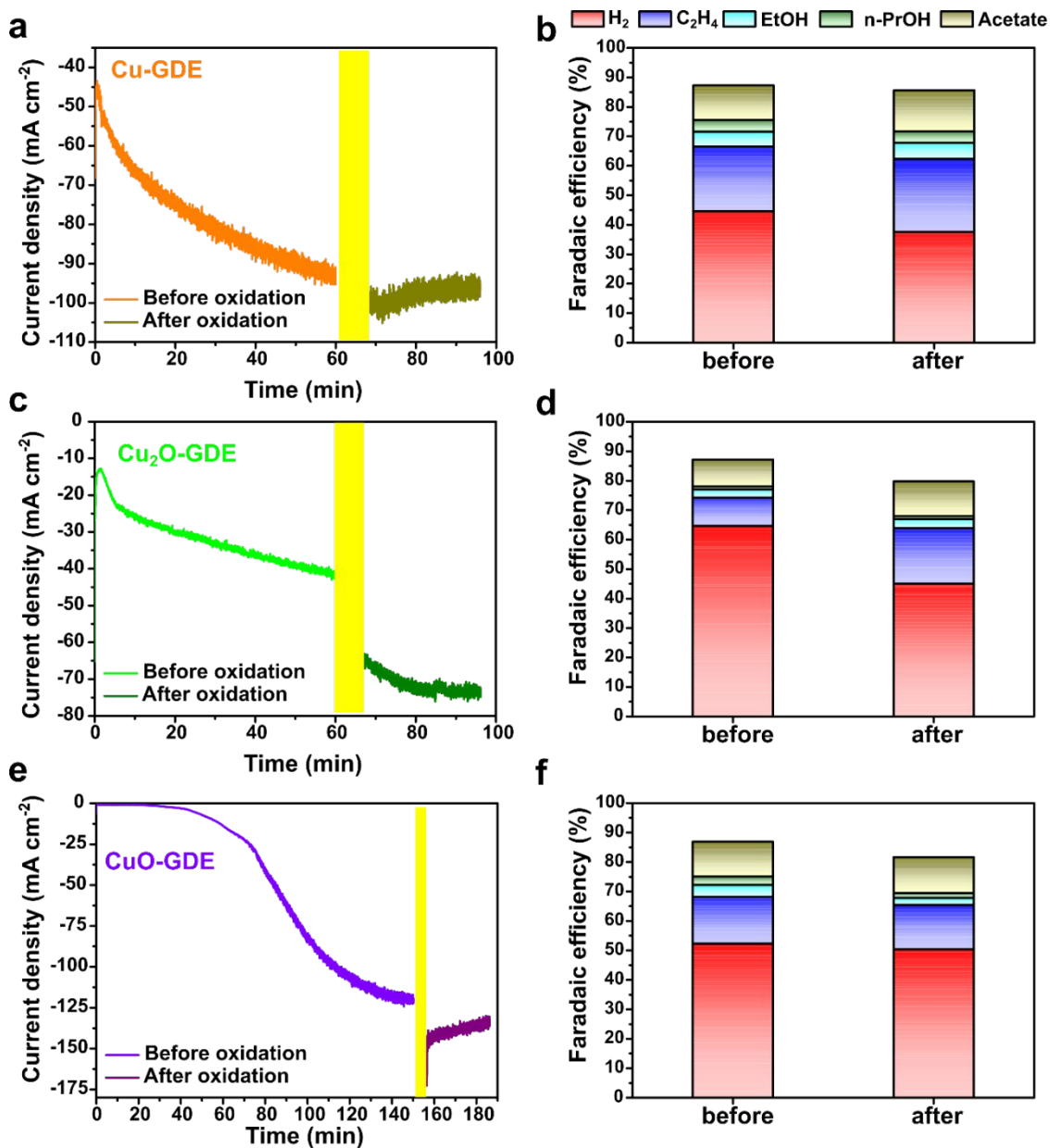TEM images of Cu-GDE before and after electrolysis and subsequent electrochemical oxidation, and (d~f) corresponding fast Fourier transform (FFT) images. In the as-prepared Cu-GDE before CORR, the $Cu_2O(111)$ phase is observed in the FFT pattern, which is matched with the XRD result. However, we also detect the CuO phase at the surface, attributed to the formation of a native oxide layer. This CuO phase can only be observed in the local area probed by TEM, not in the long-range order probed by XRD, indicating that the as-synthesized Cu-GDE could be oxidized when it is exposed to ambient air and Cu^{2+} could be generated in the local surface area. This result suggests that *ex-situ* characterization could contain oxide artifacts, highlighting the importance of *operando* studies.
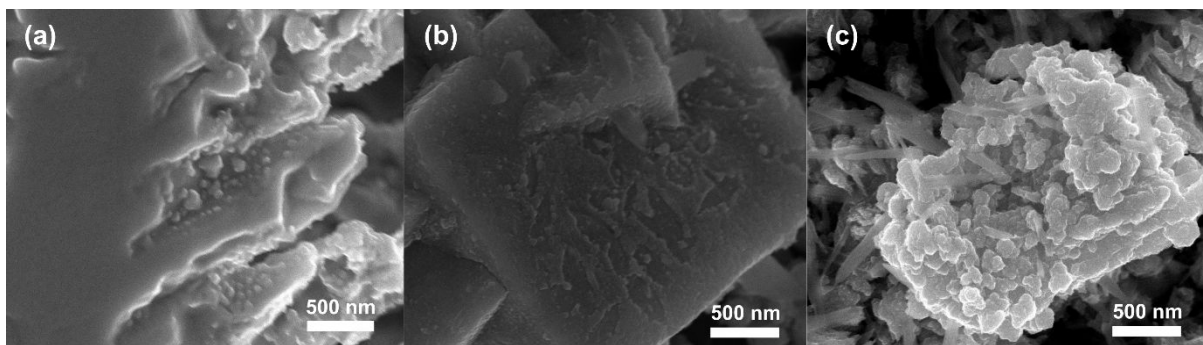
Figure S16. Morphological transformation during the second period of CORR. SEM images of Cu-GDE (a), Cu_2O-GDE (b), and CuO-GDE (c) after the second period of CORR under -2.2 V vs. Ag/AgCl. The newly formed nanoparticles on the surface coalesced into a smooth surface. Although nanocubes in the CuO-GDE were fragmented due to rapid reduction during the second CORR, the nanoparticles formed by anodic oxidation were aggregated into larger nanostructures that indicate the coalescence of nanoparticles.
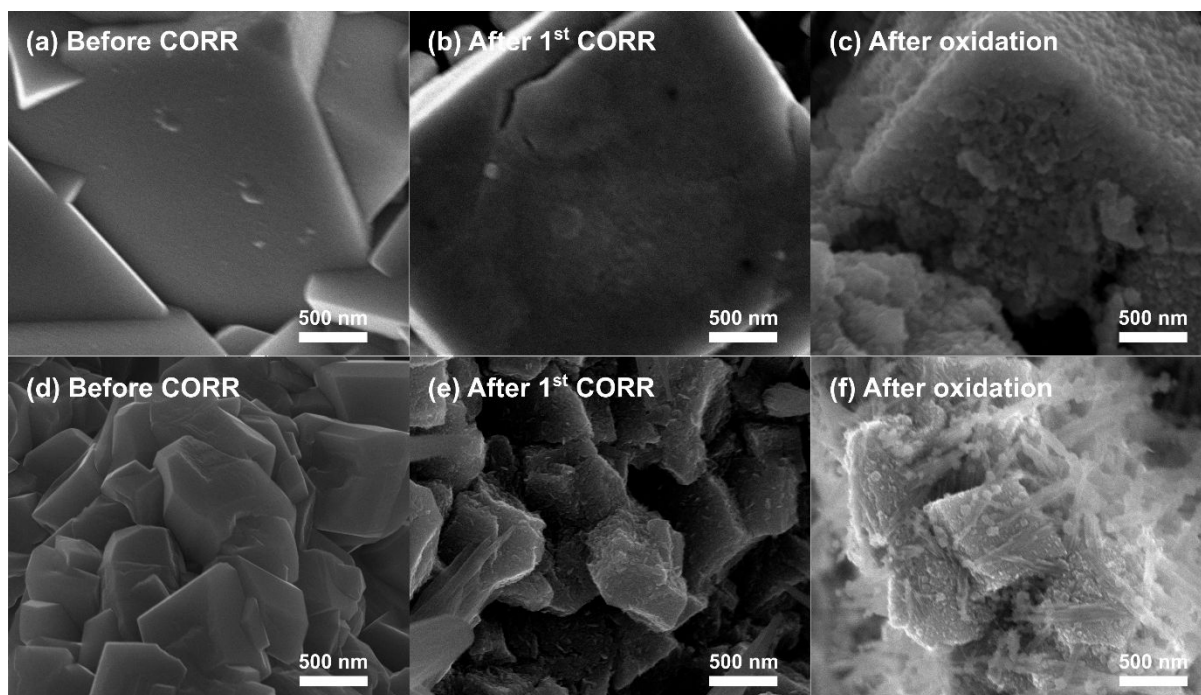
Figure S17. Morphological transformation during CORR and electrochemical oxidation. SEM images of Cu_2O-GDE (a-c) and CuO-GDE (d-f) before and after electrolysis and subsequent electrochemical oxidation. The CORR was conducted under -2.2 V vs. Ag/AgCl for 60 min, and anodic potential of 1.5 V vs. Ag/AgCl was applied for 5 min for the electrochemical oxidation.

Figure S18. Comparison of CORR performance of Cu catalysts before and after electrochemical oxidation at 0.1 V vs. Ag/AgCl for 5 min. Temporal changes of total current densities and cumulative FE of Cu-GDE (a and b), Cu_2O-GDE (c and d), and CuO-GDE (e and f). The yellow regions in the panel a,c, and e indicate the electrochemical oxidation process.

Table S1. Parameters for over-absorption correction and linear combination fitting analysis for *operando* XANES spectra of Cu-GDE under CORR at -2.2 V vs. Ag/AgCl as a representative example.

Time (min)	$\alpha*$ (a.u.)	Cu (%)	Cu_2O (%)	CuO (%)	$Cu(OH)_2$ (%)	N.S.S. (a.u.)
0	0.55	73.60	26.40	0	0	1.95e-05
	0.59	74.95	25.05	0	0	1.73e-05
	0.63	76.27	23.73	0	0	2.45e-05
6	0.55	87.13	12.87	0	0	1.42e-05
	0.59	88.61	11.40	0	0	2.18e-05
	0.51	85.58	14.42	0	0	1.63e-05
12	0.55	87.13	12.87	0	0	9.20e-06
	0.59	88.61	11.39	0	0	1.49e-05
	0.55	87.13	12.87	0	0	1.31e-05

$\alpha*$ = Over-absorption parameter

To estimate the error range in the LCF analysis, we firstly consider over-absorption correction that includes an empirical parameter. Since the over-absorption parameter (a) is an empirical value to correct this effect, we can estimate the fitting errors by varying the (a) values in one spectrum.

Table S2. Electrochemical surface area (ECSA) of Cu catalysts based on the electrochemical double-layer capacitance.

Electrode	Electrochemical surface area (cm^{-2})		
	At OCV	After CORR	After oxidation
Cu-GDE	74.45	141.02	84.76
Cu_2O-GDE	13.84	127.23	92.35
CuO-GDE	12.37	460.7	401.23

Table S3. Faradaic efficiency of product distribution of Cu catalysts before and after electrochemical oxidation at 0.1 V vs. Ag/AgCl for 5 min. The CORR performances of Cu catalysts in the previous study using the same cell configuration with different conditions are included for comparison.[S6] Some liquid products can be lost to re-oxidation at the anode compartment from the membrane crossover as previously reported. We also note that electrons can also be lost due to the reduction of surface and bulk oxide phases, as observed from the *operando* measurements.

Electrode	Treatment	Faradaic efficiency (%)					
		H_2	C_2H_4	EtOH	n-PrOH	Acetate	Total
Cu-GDE	Before oxidation	44.55	21.95	5.07	3.97	11.75	87.29
	After oxidation	37.50	24.80	5.50	3.82	14.04	85.65
Cu_2O-GDE	Before oxidation	64.58	9.69	2.78	0.94	9.19	87.18
	After oxidation	45.00	18.91	3.07	0.94	11.84	79.76
CuO-GDE	Before oxidation	52.31	15.75	4.16	2.78	11.87	86.87
	After oxidation	50.41	15.00	2.37	1.69	12.18	81.65
Cu-GDE*	50% Relative humidity	39.2	24.96	6.55	4.68	12.81	88.2
	100% Relative humidity	37.74	25.28	5.41	4.50	13.21	86.14

* The FE data in the previous report that using the same cell with different conditions.[S6]

References

S1.   Pfalzer, P.; Urbach, J. P.; Klemm, M.; Horn, S.; denBoer, M. L.; Frenkel, A. I.; Kirkland, J. P. Elimination of self-absorption in fluorescence hard-x-ray absorption spectra *Phys. Rev. B*, **1999**, *60*, 9335-9339.

S2.   Sarret, G.; Isaure, M.-P.; Marcus, M. A.; Harada, E.; Choi, Y.-E.; Pairis, S.; Fakra, S.; Manceau, A., Chemical forms of calcium in Ca,Zn- and Ca,Cd-containing grains excreted by tobacco trichomes. *Can. J. Chem.* **2007,** *85* (10), 738-746.

S3.   Manceau, A.; Marcus, M. A.; Grangeon, S. Determination of Mn valence states in mixed-valent manganates by XANES spectroscopy. *Am. Mineral.* **2012,** *97*, 816-827.

S4.   Zahiri, B.; Sow, P. K.; Kung, C. H.; Mérida, W., Active Control over the Wettability from Superhydrophobic to Superhydrophilic by Electrochemically Altering the Oxidation State in a Low Voltage Range. *Adv. Mater. Interfaces* **2017,** *4* (12), 1700121.

S5.   Liu, W.; Xu, Q.; Han, J.; Chen, X.; Min, Y., A novel combination approach for the preparation of superhydrophobic surface on copper and the consequent corrosion resistance. *Corros. Sci.* **2016,** *110*, 105-113.

S6.   Sullivan, I.; Han, L.; Lee, S. H.; Lin, M.; Larson, D. M.; Drisdell, W. S.; Xiang, C. A Hybrid Catalyst-Bonded Membrane Device for Electrochemical Carbon Monoxide Reduction at Different Relative Humidities. *ACS Sustainable Chem. Eng.* **2019,** *7*, 16964-16970.